3D analysis of equally X-ray attenuating mineralogical phases utilizing a correlative tomographic workflow across multiple length scales

Silvan Englisch[a], Ralf Ditscherlein[b], Tom Kirstein[c], Leonard Hansen[d], Orkun Furat[c], Dominik Drobek[a], Thomas Leißner[b], Benjamin Apeleo Zubiri[a,*], Alfred P. Weber[d], Volker Schmidt[c], Urs A. Peuker[b], and Erdmann Spiecker[a,*]

[a]*Institute of Micro- and Nanostructure Research (IMN) & Center for Nanoanalysis and Electron Microscopy (CENEM), Interdisciplinary Center for Nanostructured Films (IZNF), Friedrich-Alexander-Universität Erlangen-Nürnberg (FAU), Cauerstr. 3, 91058 Erlangen, Germany*

[b]*Institute of Mechanical Process Engineering and Mineral Processing, Technische Universität Bergakademie Freiberg, 09599 Freiberg, Germany*

[c]*Institute of Stochastics, Ulm University, 89069 Ulm, Germany*

[d]*Institute of Particle Technology, Clausthal University of Technology, 38678 Clausthal-Zellerfeld, Germany*

[e]*corresponding authors: erdmann.spiecker@fau.de, benjamin.apeleo.zubiri@fau.de*

Abstract

A correlative 3D characterization workflow by micro and nano X-ray computed tomography (Micro-CT, Nano-CT) and analytical scanning electron microscopy (SEM) is presented over different length scales for particle composite materials that apply to any powder at the size scale between 0.3 µm to 15 µm. In this case study, an artificial compound of calcite, talcum, dolomite, and magnesite providing constituent particles with similar morphology, size distribution, and chemical composition for multidimensional separation processes is analyzed. First, Micro-CT characterizes the particle morphology and distribution of a larger amalgamated volume. Then, a smaller, site-specifically prepared pillar is imaged by Nano-CT allowing for correlative investigations at higher-resolution. Afterwards, the Nano-CT reconstruction is informed slice-wise by analytical SEM distinguishing particles with different chemical composition. The statistical interpretation of our results is improved by advanced post-processing and multidimensional analysis, allowing for quantitative characterization of the particles' size, phase distribution, and mineral degree of liberation.

Keywords: Multidimensional particle characterization, multiscale X-ray tomography, correlative 3D analysis, statistical image analysis, parametric copula

1. Introduction

High-grade ore deposits become increasingly rare and the existing ones are more and more depleted. This tendency is not new [1] but is clearly intensifying with the increasing need for natural resources [2]. The pressure to mine ores that are significantly more complex in their structure than easily accessible material of the same quality is rising. This means that a greater variety of grain size and mineralogical neighboring phases occur in one single particle. At the same time, the requirements for the final product remain the same or even increase. In this regard, standard separation methods reach their limits or even fail if the particle properties are very similar to each other and separation is hardly or no longer possible. Moreover, complexity increases due to a multitude of new and more accurate measurement methods such as advanced microbeam techniques, which are ideally brought into correlation with each other [3]. In this context, three-dimensional (3D) measurement routines become more and more important, since they enable the precise analysis of complex particle morphologies and 3D spatial distribution at the same time.

Besides morphological and chemical composition, the steadily decreasing particle size brings up further challenges. In addition to traditional particle size characterization methods like sieving or laser diffraction measurements, which are always dependent on given class size or specific model assumptions to compute distributions from raw data, direct imaging methods are widely used to reveal multiple particle characteristics at once. Static two-dimensional (2D) imaging methods, such as light microscopy, were supplemented by dynamic methods such as dynamic light scattering [4] representing a significant development, especially with regard to the statistical representativeness of the samples [5]. Additional image tracking algorithms were used to compensate for the stereological bias [6] from the 2D image description, but only down to particle sizes of around 100 µm [7]. With these methods, a comprehensive 3D description of particle collectives smaller than 10 µm, as we focus on in this case study, is not possible. Thus, the extension to direct 3D measurement methods is needed to acquire morphological characteristics

*Corresponding authors
Email address: erdmann.spiecker@fau.de, benjamin.apeleo.zubiri@fau.de (Benjamin Apeleo Zubiri)

as well.

During the last three decades, X-ray computed tomography (CT) has become a standard tool in many research areas, like materials science [8] and geoscience [9, 10]. In particle technology, in 1992 first analyses were conducted in mineral processing on a limited number of particles with sizes down to 100 µm or in the non-particle-discrete analysis of particulate suspensions in separators, e.g., with a hydrocyclone [11, 12]. These measurements are typically based on absorption contrast where the local X-ray attenuation in projection is detected depending on the local sample thickness and material composition (X-ray attenuation coefficients), so that existing phases with sufficient difference in atomic number can be discriminated [13, 14]. To be able to reconstruct the sample in 3D, many projections under different viewing angles need to be acquired. Therefore, the sample in the stable beam path is typically rotated by the sample stage of the CT instrument within a tilt-angle range of at least 180° using a predefined tilt increment. There are several beam geometries available, two of which are used in the present study: a (quasi) monochromatic parallel X-ray beam in Nano-CT and a cone-shaped polychromatic X-ray beam in the case of Micro-CT. [15]. In both cases, the photon intensities on the detector are translated into gray-scale value images. The series of projection images is then used to reconstruct the 3D volumetric image by applying a mathematical reconstruction algorithm [15]. In absorption contrast, the gray values in the reconstructed volumes resemble the local attenuation coefficients, which can be utilized using 3D image processing routines to identify and segment different phases and extract valuable morphological and chemical information [15]. This kind of intuitive data analysis is not possible in the case of a polychromatic X-ray beam or insufficient contrast due to similar attenuation coefficient of the constituent phases of the sample, so that additional information for a robust segmentation is required.

In the case of powders with particles consisting of different phases, another key parameter besides the particle-discrete information is the phase-discrete information. The combination of both can offer a detailed characterization of the particle and batch composition. It is noteworthy to say that a particle may consist of several grains, which in this context refers to a volume containing a single mineral phase. In the field of mineral processing, one distinguishes, for example, between valuable grains (or phases) and non-valuable grains within particles to ascertain how well the valuable materials can be enriched. The volume ratio of all particles, which consist of only the valuable phase, to the total of all particles, which contain this specific phase is called liberation degree (LD). The LD is an important but aggregated parameter for the processing (e.g., milling or separation processes) of primary and secondary mineral raw materials. In the present study, the 3D particle-discrete determination of the LD will be shown as a concrete application example for the use of the correlated particle-discrete and grain-discrete data. In contrast to existing studies [16], this is demonstrated here using an example of X-ray attenuating mineral phases with comparable X-ray attenuation contained in particles smaller than 10 µm.

A standard measurement set-up for a 2D determination of the mineralogical composition on polished epoxy-embedded sections, i.e. the mineral liberation analysis (MLA) [17], consists of scanning electron microscopy (SEM) using the back-scattered electron (BSE) signal in combination with an energy dispersive X-ray spectroscopy (EDXS) detector for elemental analysis. A computer software in combination with databases on known materials can now be used to identify the containing minerals and provide a color image, where each color corresponds to a certain mineral. It is typically difficult to correct for the discrepancy in analysis results of 2D sectional images compared to results obtained by the analysis of real 3D structures, called stereological bias [6]. Even with an optimized sample preparation strategy to suppress segregation effects due to sedimentation [18, 19], the influence of the particle's internal structure is significant [20]. With the presented 3D methodology, it will be possible to discretely perform this liberation analysis of multiphase particle systems. Previous studies have done this, e.g., for binary systems [21], or for other particle size scales of around 100 µm [16].

The shape of particles is often correlated with the mineralogical composition of particles [22]. In some cases, this allows for a mineralogical characterization by means of particle shape characteristics, which can easily be determined from CT data. However, if distributions of 3D morphological particle descriptors overlap, there is a need for additional phase-specific information to guarantee a valid identification, especially in terms of mineralogical phases. Already established workflows can be used (i) to distinguish between phases with strongly differing attenuating properties, e.g., gold phase in other mineralogical components. Here, the qualitative difference is clearly visible in the gray value histogram and can be used for direct phase identification [23]. Another workflow is (ii) to use characteristic, element-specific absorption properties, where a sample is scanned with two different energies slightly above and below a phase specific discontinuity in the absorption behavior, e.g., a X-ray absorption K-edge of the elements in one known phase of interest [24]. A relatively new workflow is (iii) to use an additional energy-dispersive detector, called spectral CT, which is able to distinguish between multiple phases at once [25].

The alternative, new workflow proposed in the present study possesses the following advantages in comparison to the existing workflows (i)-(iii) mentioned above. It enables to distinguish between mineral components of a micron-sized particle system having comparable X-ray attenuating properties and consisting of more than one phase. Furthermore, our workflow can be implemented with existing lab-based CT devices without the need for an extension by an additional detector. Note that our workflow uses additional prior information regarding local chemi-

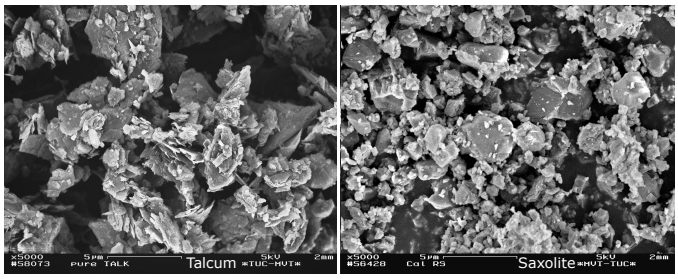

Figure 1: Particle systems considered in this study, (left) talcum with three different sub-phases of dolomite, magnesite, and talcum; (right) saxolite.

Table 1: Chemistry and density of the two particle systems saxolite and talcum, the latter consists of three different sub-phases, which are dolomite, magnesite and talcum. Attenuation at 5.4 keV represents the attenuation length within a given material of the quasi-monochromatic Nano-CT beam.

	Chemistry	Density in $g \cdot cm^{-3}$	Attenuation at 5.4 keV
Saxolite	$CaCO_3$	2.75	15.3 µm
Talcum			
Dolomite	$MgCa(CO_3)_2$	2.86	23.5 µm
Magnesite	$MgCO_3$	3.00	55.4 µm
Talcum	$Mg_3Si_4O_{10}(OH)_2$	2.76	34.7 µm

cal composition from EDXS, which was performed in a similar way in Furat et al. [26] covering particle sizes of 315 µm to 500 µm. In the present study, their method is extended to particle sizes below 10 µm by correlating Micro-CT measurements of medium-resolution (∼700 nm) with high-resolution (∼150 nm) measurements, which are conducted using a combination of Nano-CT, SEM imaging and SEM-EDXS, where specific slices in the Nano-CT volume are accessed using focused ion beam (FIB) milling. This correlative measurement routine enables examinations over multiple length scales with a consistent and adaptable analysis and preparation workflow.

The paper is structured as follows. In Sec. 2, we shortly introduce the considered particle system, describe the measurement workflow for volume correlation followed by the applied image processing strategies and data analysis methods. In Sec. 3, we present the results of the correlation between the Nano-CT volumes and the cut sections from the FIB-SEM-EDXS analysis, and the phase determination for materials characterization. In Sec. 4, we discuss the results with respect to the precision of the derived quantitative data as well as its reliability concerning a larger scale. We then close the loop to practical applications by discussing the benefits of our correlative workflow to tackle the challenges of separation processes. In Sec. 5, we summarize the advantages of the presented workflow in terms of statistical significance and the 3D particle-discrete and grain-discrete provision of the analysis results compared to conventional 2D methods.

2. Materials and Methods

2.1. Particle System

The materials considered in this study are natural products and therefore differ in their purity and homogeneity. Saxolite, type Saxolith®2 extra, was received from the Erzgebirgische Kalkwerke GmbH GEOMIN, Germany. Talcum was received from Giessereitechnik Wystrach GmbH & Co. KG, Germany. Exemplary SEM images of these materials are shown in Fig. 1.

The corresponding particle size distributions of saxolite determined by laser diffraction and of talcum particles determined by sedimentation analysis can be found in the Supplementary material. The distributions overlap in large parts between 1 µm to 10 µm in diameter, showing that particle size alone is not fully suitable as a separating characteristic. As it can be seen in Tab. 1, also the densities do not differ significantly. Considering talcum as a mixture with a mean density from the tabulated values for dolomite, magnesite and talcum, this becomes even clearer. Additionally, some saxolite particles are composites which contain traces of talcum (up to 4 %), making it even harder to identify these materials. Assuming comparable particle sizes, a distinction between the two phases on the basis of the gray-scale histograms from both Micro-CT and Nano-CT measurements is not possible.

For the creation of a suitable and valid analysis workflow, a mixture of both particle systems (talcum and saxolite) was manufactured. A mixing ratio of 30 to 70 (volume fraction) was chosen as an expected scenario for a future application of the analysis workflow, in our case, the characterization of a multidimensional separation with respect to two (including the sub-phases, four) particle characteristics. The separation itself is realized by a combination of a deflector wheel classifier (separation by size) and a triboelectric charging process due to particle wall collisions (separation by charge) [27]. The various mineral components carry different charges due to their triboelectric characteristics, e.g., their electrochemical potential, so that they can be separated by their electrical mobility.

2.2. Measurement Workflow for Volume Correlation

The following workflow is a correlative study across different X-ray and electron microscopes. Every microscope adds information by utilizing its advantages of the capable sample size, achievable resolution and information content (morphological, chemical). The scale bridging nature is necessary to determine the coordinates for further processing with the help of laser ablation and to ensure the representativeness of the individual volumes of high-resolution scans using Nano-CT. The low-resolution measurements performed with Micro-CT are used to determine the homogeneity of the particle dispersion of the initial sample and to check its suitability (absence of cracks and air bubbles) for the subsequent sample preparation workflow by laser ablation and FIB-SEM.

2.2.1. Sample Preparation

To guarantee a well-dispersed homogeneous sample, the particles are mixed with low X-ray attenuating carbon black nanoparticles acting as spacers. Touching particles are a potential source for errors in the image processing workflow when separating to create particle-discrete data sets, which are essential for further quantitative analyses. For a detailed description of the sample preparation method, see Ditscherlein et al.[19]. The epoxy-carbon black matrix is well machinable, using mechanical preparation techniques as well as using high-energy radiation techniques, e.g., laser ablation to create sample volumes for Nano-CT experiments and FIB to cut sections for correlative SEM measurements.

2.2.2. Micro-CT Measurements

Micro-CT scans were performed using a Zeiss Xradia 510 Versa, with a polychromatic X-ray source, a rotating tungsten target, a maximum acceleration voltage of 160 keV, and a maximum power of 10 W. Compared to conventional Micro-CT systems, where the magnification is determined by the geometrical arrangement of source, sample and detector, an additional magnifying optic (factors 0.4x, 4x, 20x, 40x) allows a minimum voxel size of 0.3 µm. The Micro-CT scans were performed on a manually cut bar (see Sec. 2.2.1) using two different magnifications (see Tab. S2) – one lower resolution overview scan to check the Micro-CT sample for possible preparation artifacts, and one medium resolution scan to confirm the representativeness and homogeneity of the particle dispersion and to obtain the coordinates for the subsequent high-resolution Nano-CT scans, see Fig. 2. Since the applied preparation method cannot completely prevent the incorporation of air bubbles into the matrix, bubble-free regions can also be identified here that are suitable for further preparation with the laser ablation system to create cylinders for the high-resolution Nano-CT scans.

2.2.3. Laser Ablation

After the Micro-CT experiments, the sample size was further reduced for Nano-CT investigations using a 3D-Micromac microPREP™ PRO laser ablation system. The sample top region was ablated down from a manually cut bar of 400 µm to a pillar with 60 µm in diameter, see Fig. S3, which fits into the field of view (FOV) of the Nano-CT instrument. For both Micro-CT and Nano-CT machines, which were used in this work, the detectors have a certain number of pixels and therefore a static FOV for each pre-defined magnification setting. This leads to a fixed captured volume, where the sample size should match the FOV at best to avoid reconstruction artifacts due to interior tomography restrictions [28]. Along the length of the pillar, the FOV can easily extended by acquiring multiple tomographic tilt series along the vertical axis.

2.2.4. Nano-CT Measurements

High-resolution 3D scans were performed using a Zeiss Xradia 810 Ultra Nano-CT instrument, which operates with quasi-monochromatic X-rays at constant photon energy with parallel beam geometry. The quasi-monochromatic beam is a result of the filtering properties by the microscope's X-ray optics containing a condenser and a Fresnel zone plate lens that attenuate certain wavelengths due to their dispersion efficiency. The lenses are optimized to transmit an even narrower bandwidth of the characteristic X-rays. In this case, X-rays with an energy of 5.4 keV are used corresponding to the characteristic X-ray energy of the Kα-line of a rotating chromium anode. We utilize absorption contrast mode which exhibits mainly mass-thickness contrast imaging with a minimum voxel size of 64 nm. The quasi-monochromatic X-rays allow a direct correlation of the reconstructed image intensities to local attenuation coefficients, which manifests itself in the different brightness of the particles in slices of the reconstructed tomograms. Volume reconstruction based on simultaneous iterative reconstruction technique (SIRT) was performed with an in-house Python script based on the algorithms provided by the ASTRA toolbox [29, 30, 31]. The high-resolution scans are needed to acquire the 3D particle-discrete information of the whole volume, which is a combination of three vertically stacked individual volumes (see Fig. S4(b) for the positions of the single Nano-CT reconstructions indicated in the complete, stitched Nano-CT volume). Detailed measurement parameters of the tomographic measurements can be found in the supplementary material table S2.

2.2.5. FIB Preparation, SEM Imaging and SEM-EDXS

FIB milling, SEM imaging and energy dispersive X-ray spectroscopy (EDXS) were conducted in a FEI Helios NanoLab 660 SEM/FIB dual-beam system. For the FIB milling process, which is used for the preparation of thinner and finer Nano-CT sample pillars, Ga+ ions with high kinetic energy are directed onto the sample surface to achieve local material ablation. The 60 µm pillar was cut vertically along the rotation axis in order to remove the melting zone of the laser ablation. As described in Section 2.2.4, the sample has been imaged in 3D at three positions by acquiring Nano-CT tilt series (see Fig. S4(b) for the slice positions indicated in the complete, stitched Nano-CT volume). Thus, the sample was sliced in the regions of each of these three corresponding Nano-CT data sets with 28° horizontal inclination (limited by the SEM/FIB stage) and imaged after each cut. Charging effects during the milling process are common with these minerals. Thus, each cut is processed in a single run. A connected secondary electron (SE) detector provides the image data of the current sectional plane surface. Backscattered electron (BSE) imaging and EDXS of the same cut surfaces make it possible to distinguish between the talcum sub-phases and saxolite, by providing additional information about the local chemical composi-

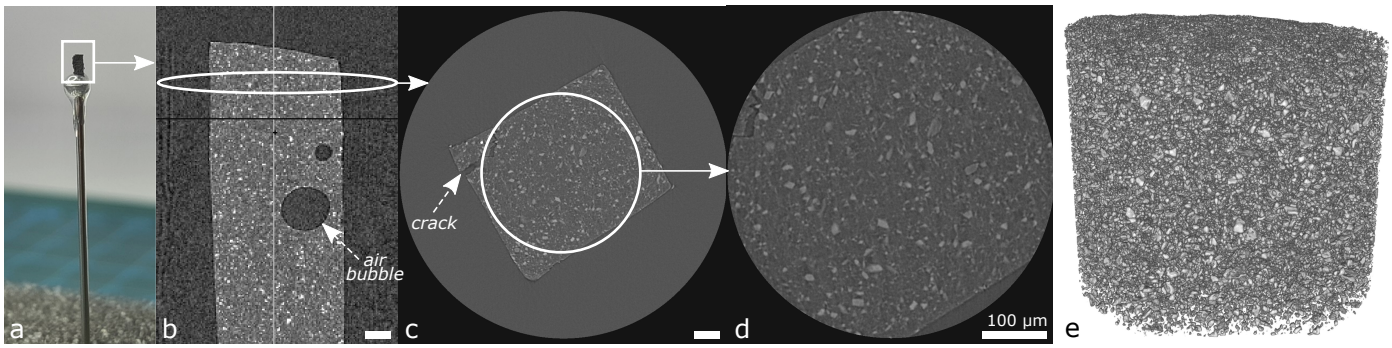

Figure 2: Mechanically dispersed particle system embedded in an epoxy-carbon black matrix, see [19] for a detailed description of the preparation, (a) glued on a needle pin, scanned with low resolution by Micro-CT, represented here by (b) a side view and (c) an exemplary horizontal slice through the reconstructed volume (d) to validate the homogeneity of the sample without air bubbles and to get the coordinates as a starting point for a follow-up laser ablation process to create a cylinder for high-resolution measurement by Nano-CT and FIB-SEM.(e) 3D rendering of reconstructed medium resolution Micro-CT. Note that the indicated scale bars are referring to the same measure of 100 µm.

tion enabling a subsequent detailed phase analysis, which was not possible with gray-value based analysis methods only.

2.3. Image Processing Strategies

As already mentioned in Sec. 2.2, the described sample preparation workflow is strongly supported by a detailed image processing strategy to allow for a robust identification and segmentation of particles consisting of different constituent materials. In contrast to the workflow presented in Ditscherlein et al.[32], where single phase information is used to create particle-discrete data sets, in the current study, the particles consist of different mineral phases, i.e., grains of different chemical composition. Thus, the novelty of the present approach is the combination of a phase-discrete and an enhanced particle-discrete workflow. The results from the phase-discrete and the particle-discrete analysis are based on different image processing workflows and, therefore, can be clearly separated from each other as described in the next two sections. The results of both approaches are merged in Sec. 3, to describe the data sets in a meaningful way with regard to their distributed descriptors.

2.3.1. Nano-CT Phase Segmentation

The BSE and EDXS analysis from the FIB slices was utilized to add information to the Nano-CT data set segmentation, according to the routine described by Lenz et al. [33]. This was conducted in the commercial software Arivis Vision4D with a machine learning algorithm based on ilastik [34]. The EDXS analysis was used as ground truth. Large phases, which could accurately be allocated in the EDXS maps, were identified in the corresponding Nano-CT slices and then manually segmented to train the machine learning algorithm, as illustrated in Fig. 7(c). To avoid an overlapping of regions of darker contrast in the Nano-CT reconstruction, whose contrast is affected by edge gradients of brighter particles due to the optical resolution limit of about 150 nm, the separation threshold was set in such a way that it is able to separate the particles from each other. Manual color segmentation and, in particular, the threshold were adjusted until the resulting segmentation matched the corresponding EDXS analysis (cf. Figs. 7(d-e)). The difference between EDXS and segmented data was judged by visual inspection. Additionally, the Intersection over Union (IoU) [35] was determined on single-phase particles of adjacent slices as test data to the original training data to obtain a quantitative measure for the precision of the phase segmentation. The phases were color segmented manually in the slices of the test data and compared with the segmented data from the training. The IoU was calculated using the ratio of the overlap to the union of both data using $\mathrm{IoU} = \frac{area_{overlap}}{area_{union}}$. In the manuscript, the segmented phases contained in each particle are referred to as grains of the particle and are counted individually for the later analysis, see Fig. 10. So, a single particle can contain multiple grains of the same phase. The individual particles are characterized by the image processing procedure described in the following section.

2.3.2. Nano-CT Particle Segmentation

In order to subsequently analyze the characteristics of particles, an image segmentation procedure was deployed which partitions the Nano-CT image data into regions corresponding to individual particles. The segmentation workflow is illustrated in Fig. 3. For that purpose, a fully convolutional neural network architecture was chosen, specifically an approach based on a 3D U-net (see the illustration in Fig. S5) is used, cf. [36, 37]. For the training of this network, three separate Nano-CT slices were annotated manually (each with around 100 individual particles) and used as ground truth. After training, the network is applied to the Nano-CT volume, and after binarizing the output of the trained network, individual particles are separated and can be identified by finding the connected components, see Fig. S6. As can be seen in Fig. 3, the manual annotation of the training data introduces inaccuracies that impact the network output, especially with respect to

particle size and shape in areas where particles interface. Therefore, to capture the particle size and shape more accurately, a marker-based watershed algorithm is applied to the binarized CT image data, using the connected components of the initial segmentation as markers, see [38]. Further details on the network architecture and training procedure can be found in [37].

2.3.3. Micro-CT Particle Segmentation

The phase and particle characterization emits in this study mainly from the Nano-CT reconstructions. To estimate the local representativeness of the measured Nano-CT volumes with respect to homogeneity, the Micro-CT reconstruction was utilized to bridge the scale of the particle characterization towards larger dimensions. Here, the Micro-CT volume was segmented by the machine learning algorithm based on ilastik [34] similar to the Nano-CT phase segmentation routine, but targeting only the particle size without phase information.

2.3.4. Mineral Liberation

As mentioned in the previous sections, a particle can consist of several connected components of a given phase, referred to as a grains. Multiple grains of a particle phase are individually evaluated provided that they are separated from each other by another phase. The volume fraction (being equal to mass fraction due to similar densities) of a valuable mineral, denoted by i, that is present in a collective of grains in an ungrown form, i.e., in the form of free grains, is called the liberation degree and denoted by LD_i. It is given by

$$\mathrm{LD}_i = \frac{V_{i,\mathrm{free}}}{V_{i,\mathrm{free}} + V_{i,\mathrm{intergrown}}}, \tag{1}$$

where $V_{i,\mathrm{free}}$ denotes the total volume of the fully liberated particles (with volume fraction larger than 0.99) of phase i, i.e., particles consisting of only one grain of the phase i, and $V_{i,\mathrm{intergrown}}$ denotes the volume of the remainder of phase i. However, smaller particles are generally more likely to occur fully liberated. Thus, investigating size dependent liberation information is of interest. Therefore, for an interval $I \subset [0, \infty)$, i.e., a defined particle size range, the liberation degree of particles with volume in I is given by

$$\mathrm{LD}_i^I = \frac{V_{i,\mathrm{free}}^I}{V_{i,\mathrm{free}}^I + V_{i,\mathrm{intergrown}}^I}, \tag{2}$$

where $V_{i,\mathrm{free}}^I$ denotes the volume of the fully liberated particles with volume in I of phase i and $V_{i,\mathrm{intergrown}}^I$ denotes the volume of the remainder of phase i in particles with volume in I. Thus, partitioning the size range into disjoint intervals, the liberation degree can be analyzed in more detail, see Fig. 10.

Usually, the shares are determined by creating property classes, e.g. via swim-sink sorting or via 2D image analysis. However, in the letter case only area fractions are being considered instead of volume fractions.

3. Results

3.1. Correlative Microscopy Workflow

The first challenge is the identification and correlation of the minerals (particles and grains) across the different congruent reconstructed volumes or acquired slices using different tomography and imaging techniques. As can be seen in Fig. 4, the applied workflow starts with the medium-resolution Micro-CT scan of a sample with larger size of around 400 µm. In a next step, the Micro-CT pillar is site-specifically cut down using laser ablation to fit the Nano-CT's field of view of $(65\,\mu\mathrm{m})^2$ enabling a correlation with the Nano-CT reconstruction. Then, three vertically stitched high-resolution Nano-CT tilt series covering the complete Nano-CT pillar are acquired. Their subsequent 3D reconstruction is further identified and correlated with the corresponding region in the Micro-CT tomogram. In this way, a certain volume within the reconstruction obtained by Micro-CT can be displayed at higher resolution and with improved contrast. In the last preparation step, the Nano-CT pillar is FIB milled from the vertical side creating a cut parallel to the pillar axis. This enables SEM-EDXS analyes of a specific region of interest (ROI) within the pillar, so that for this ROI, measurement data from all three microscopy techniques is available and can directly be correlated, as illustrated in Fig. 4.

3.2. Precise Mineral Allocation

The distinction between minerals in the Nano-CT reconstructions can be estimated to certain extent already by the local gray values of voxels (cf. Figure 4(a-b)), since each component exhibits a specific attenuation coefficient for the 5.4 keV X-ray beam, in contrast to the Micro-CT instrument, see Tab. 1. Although the X-ray beam is quasi-monochromatic, the corresponding gray values in the 3D reconstruction for the different phases are further affected by a remaining X-ray energy dispersion, material density variations or limited resolution. Thus, local attenuation coefficients are not perfectly recovered in the 3D reconstructions, which impedes a unambiguous assignment of a certain mineralogical phase to every voxel only from gray levels. To compensate this uncertainty, we utilize local compositional information from SEM-EDXS analyses to inform the Nano-CT volumes and extrapolate the phase information from a 2D slice to a 3D reconstructed volume. This method allows for a thorough assignment and segmentation of the local mineralogical phase information to every voxel of a 3D reconstruction and therewith enables a precise identification of distinct particles and grains.

The analysis workflow with the achievable sample size and resolution of each step and technique is illustrated in Fig. 5. The sample is site-specifically sliced using the FIB with nearly horizontal cuts (slices perpendicular to

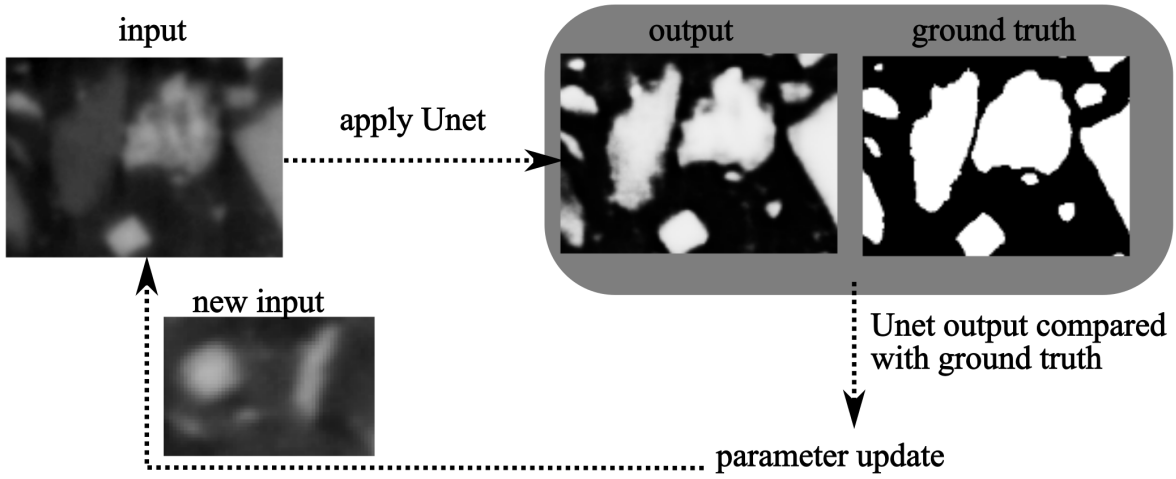

Figure 3: Exemplary particle segmentation workflow using U-nets. A grayscale image is used as input. Output, ground truth and weight map lead to a loss function. Afterwards the parameters are updated and the cycle repeats with a new image as input.

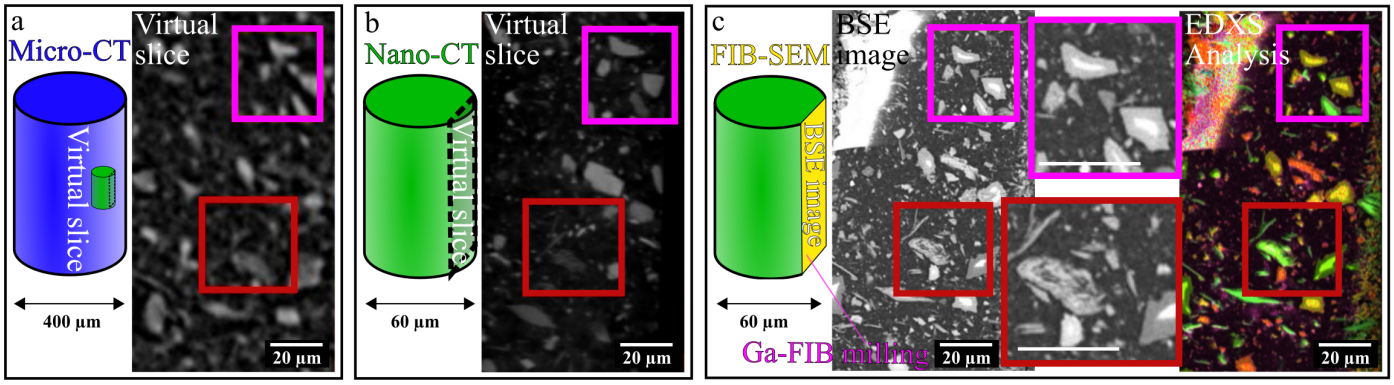

Figure 4: Correlative microscopy workflow of one identical region across multiple length scales. Virtual slices through (a) medium-resolution Micro-CT and (b) high-resolution Nano-CT reconstruction revealing the same particles as detected in (c) the BSE image after the smaller Nano-CT pillar (diameter of 60 µm) was vertically cut out of the larger Micro-CT sample. The insets illustrate the increased detail depth of the BSE images compared to the Micro-CT and Nano-CT slices. The EDXS maps (net intensities) provide additional information about the chemical composition (saxolite in red, dolomite in yellow, magnesite in green, talcum in cyan; see also Fig. 6).

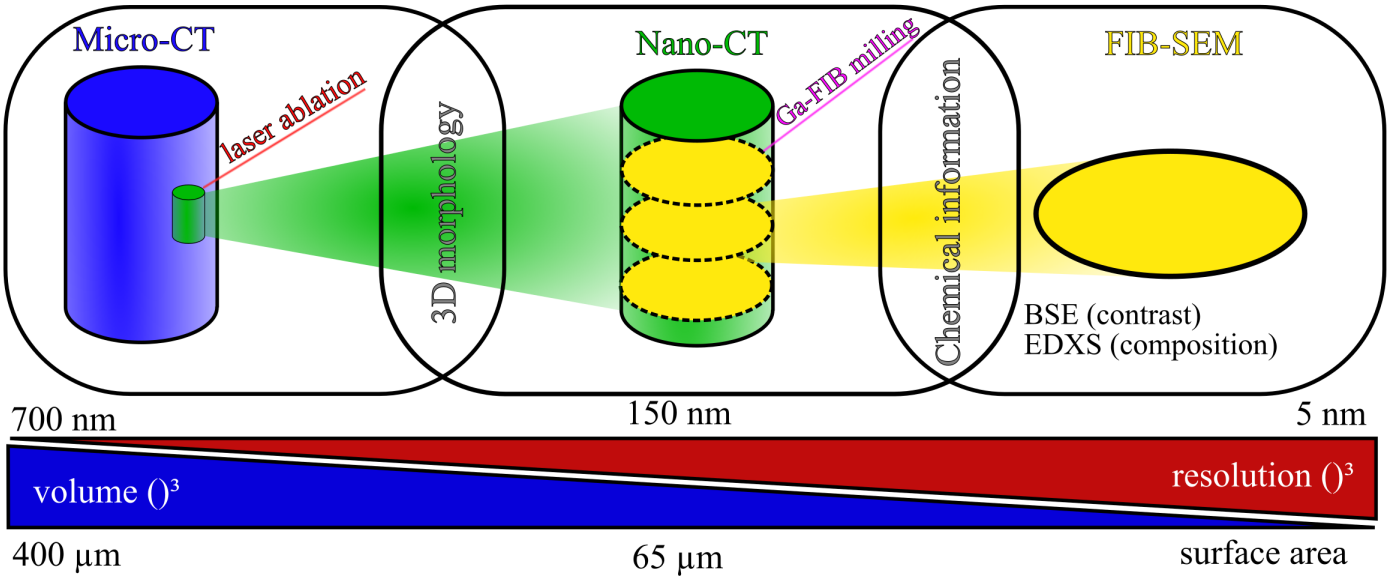

Figure 5: Correlative workflow from Micro-CT measurements of a larger volume to a sample with reduced size generated by applying laser ablation preparation suitable for Nano-CT measurements, both realistically reconstructing the 3D morphology of the particulate sample. The application of an additional milling process with FIB enables the acquisition of slices through the volumes used for Nano-CT for chemical characterization via SEM-EDXS.

the long axis of the pillar sample) and analyzed with SEM-EDXS (cf. Fig. 5 center) after the correlation of the Nano-CT volumes with the SEM image of a vertical slice through the Nano-CT pillar (cf. Fig. 4(b)). Fig. 6 depicts the SEM-EDXS analysis of an exemplary, nearly horizontal slice. The cutting heights are chosen according to interesting slices identified in the Nano-CT tomograms, where every possible constituent mineral appears to a sufficient amount enabling a reliable segmentation of all phases. In Fig. 4 (vertical slice in (b) and (c)) and Fig. 7 (horizontal slices in (d) and (f)), the same particle shape in both images proves the correctly applied correlation. The phase-discrete segmentation is processed on the horizontal slices, shown in Fig. 7 where every cut was taken from one of the three individual Nano-CT volumes. Each mineral results in a different gray-scale value (cf. Fig. 7, (c) and (f)) and can be directly matched with a combination of the EDXS signals leading to the color code used in Figs. 6 and 7, where red represents saxolite (calcite), yellow dolomite, green magnesite and cyan talcum. Fig. 6 shows (a) a BSE contrast image and element-specific EDXS maps of (c) calcium, (d) magnesium and (e) silicon with respect to the constituent minerals of one exemplary cut. This leads to the combined EDXS image in Fig. 6(b) with the same color code enabling a clear/convenient distinction between the different constituent minerals.

3.3. Volume Correlation

The element-specific EDXS signals of calcium, magnesium and silicon are analyzed with respect to the constituent minerals, as illustrated in Fig. 7(a). First, the machine learning (ML) segmentation algorithm (see Sec. 2.3.1) is trained in a selected Nano-CT slice (Fig. 7(a)) to assign every voxel of the segmented particle regions to one of the four minerals. Here, the particles in the EDXS analysis (as indicated with a blue rectangle), which are large enough to be visually allocated to the phases, are utilized for the training. The larger phases from the EDXS maps can clearly be identified and labeled in the corresponding Nano-CT slices (cf. Fig. 7(b)). Here, typically 1-3 large particles of each phase can be colored. However, the exact shape slightly differs due to surface cutting artifacts of the Ga-ion beam (beam divergence). Phases, like the yellow dolomite at the bottom of Fig. 7(c), typically also extend into z-direction (long axis of pillar) and therewith can be identified also in other nearby z-slices, around 2-5, of the Nano-CT tomogram. Likewise expands the EDXS analysis over adjacent z-slices of the Nano-CT tomogram. Thus, the manual labeling is repeated for multiple Nano-CT slices which contain the particle with known phase information from EDXS. The trained algorithm is then applied to the entire Nano-CT volume. The final results show the phase segmentation of each of the particles with respect to saxolite, dolomite, magnesite and talcum in Fig. 7(c and e). A closer look at the identified phases in the blue boxes of Figs. 7(a-c), shows that the actual composition of particles can be more complex than originally suspected. The larger red particle, for instance, had been originally identified in the manually segmented Nano-CT data set for machine learning training as one pure saxolite grain (cf. Fig. 7(b)). However, after the training with the additional SEM-EDXS data, the actual composition results in a mixture of red and yellow (saxolite and dolomite) grains, as shown in Fig. 7(c). In this way, it is possible to refine the ML algorithm until the qualitative difference by visual inspection between the ML segmentation results

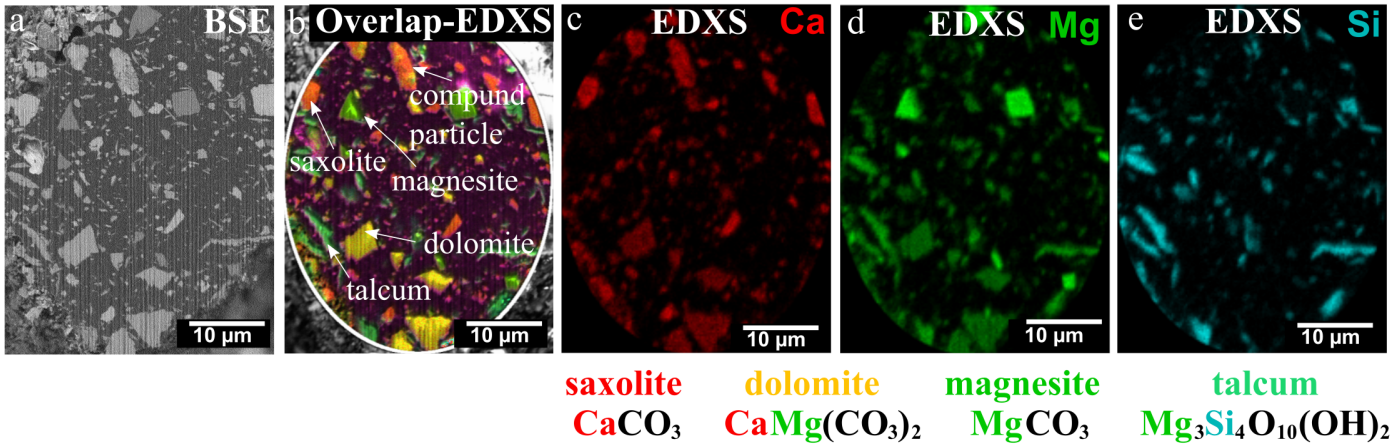

Figure 6: Mineral determination according to the chemical components. (a) BSE overview image already enables to distuinguish individual particles with different chemical composition. (c) Ca- (d) Mg- and (e) Si-EDXS analysis (net intensities) reveals the individual components in the combined image (b) with high precision. See Fig. S4(b) for the slice position indicated in the Nano-CT volume.

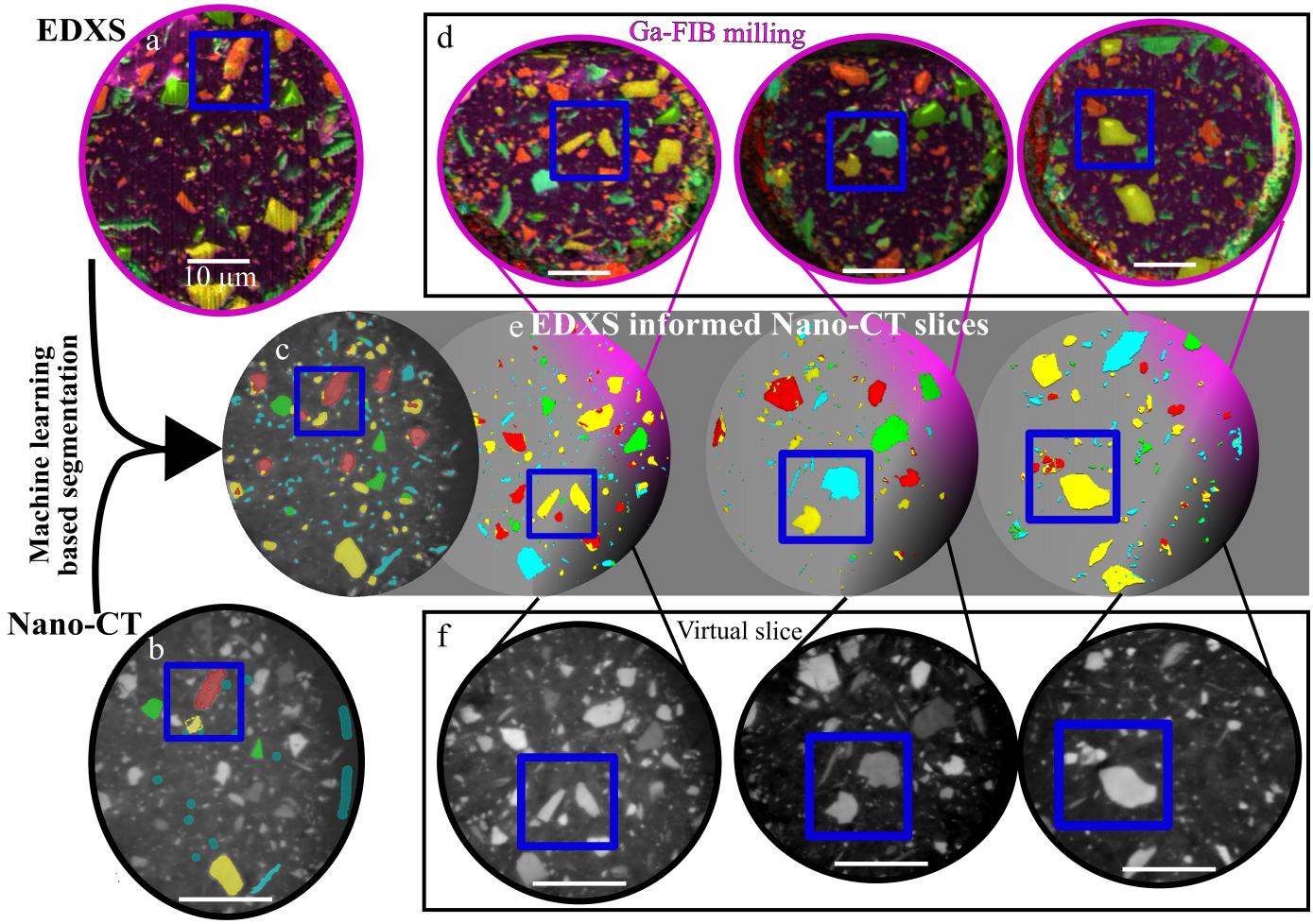

Figure 7: Phase-related segmentation workflow. (a) SEM-EDXS analysis (net intensities) reveals the distinct mineral phases through their different chemical composition (saxolite in red, dolomite in yellow, magnesite in green, talcum in cyan). (b) Virtual slice through the Nano-CT reconstruction at the same location as the corresponding EDXS map: gray scale range of each phase in Nano-CT is manually segmented to train the ML algorithm in individual slices using the EDXS signal. (c) The ML algorithm allocates the different phases first to one single slice and from this to the complete corresponding Nano-CT reconstruction. This is repeated at three other positions (one slice in each single Nano-CT reconstruction) shown in (d) and (f), leading to a phase-sensitive segmentation in (e) which is extrapolated to the full Nano-CT reconstruction, as illustrated in Fig. 8. The difference between the exact particle morphology of (d) and (f) is a result of the divergence of the focused ion beam. All scale bars represent 10 µm. See Fig. S4(b) for the slice positions and the positions of the single Nano-CT reconstructions indicated in the complete Nano-CT volume.

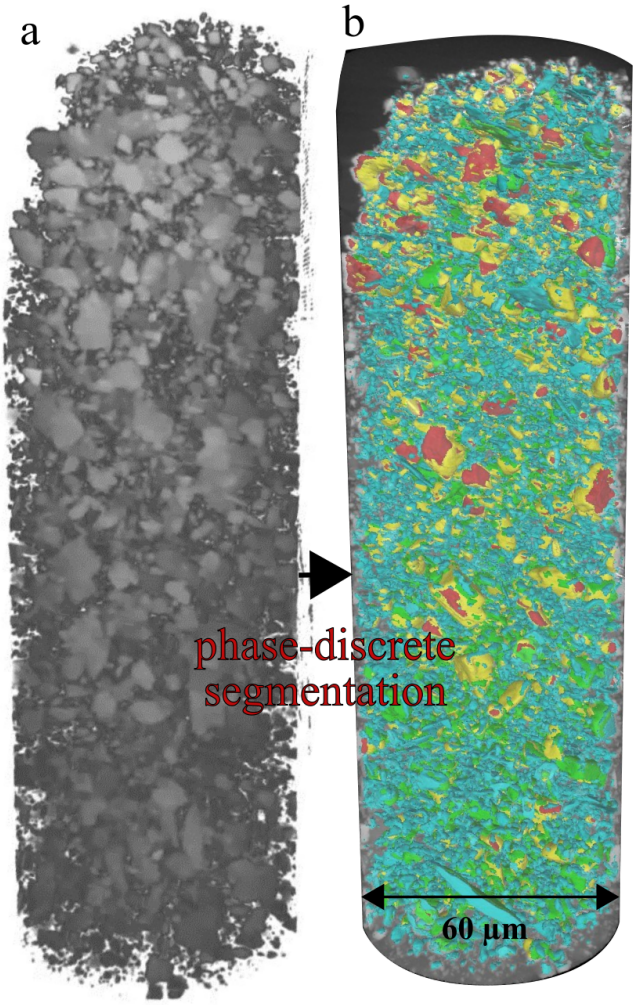

Figure 8: Three stitched Nano-CT reconstructions as gray-scale image in (a) and after phase-discrete segmentation in (b).

and the EDXS maps is minimized. To judge the refined training quantitatively, we color segmented single-phase particles of each mineral manually in an untrained z-slice and calculated the IoU of the manual and ML segmentation results. The IoU ranges between 0.95 and 0.84, with a mean value of 0.91 for the utilized particles. The final segmentation of each of the three Nano-CT volumes is illustrated in Fig. 7(d-f). The EDXS maps in Fig. 7(d) and the virtual slices in Fig. 7(f) show a good match and the resulting segmentations in the three slices in Fig. 7(e) are in a good agreement with Fig. 7(d). Lastly, as illustrated in Fig. 8(b) and in Fig. S4, the three individual segmented sub-volumes are merged to obtain the final phase-discrete segmentation of the whole Nano-CT reconstruction.

3.4. Particle-discrete Analysis

After having finished the phase-discrete segmentation, we investigate the volumes with respect to particle-discrete information. To do so, the identified regions in the Nano-CT volumes of saxolite, dolomite, talcum and magnesite are registered in the particle-wise segmentation and the

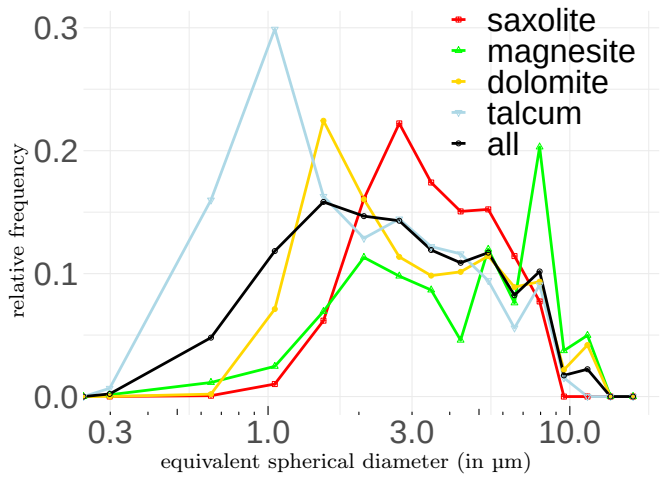

Figure 9: Mass-weighted, normalized histograms of the equivalent spherical diameter of particles which predominantly consist of one mineral (volume fraction larger than 0.5) and of all identified particles. The lower end is cut off by the resolution.

resulting mineralogical composition of individual particles is correlated to particle descriptors, such as the equivalent spherical diameter (see also the comparison of phase-discrete and particle-discrete segmentation illustrated in Fig. S6). The mineralogical composition of each particle is quantified by four scalar values, corresponding to the volume fractions of saxolite, dolomite, talcum and magnesite of the given particle. Fig. 9 depicts the mass-weighted, normalized histograms of the equivalent spherical diameter of particles which predominantly consist of one mineral (volume fraction larger than 0.5). The combination of the segmentation workflows considered in Sections 2.3.1 and 2.3.2 provides a volume ratio of 27 to 73 (saxolite to talcum + dolomite + magnesite) which is comparable to the original mixture of minerals (see Sec. 2.1) and will be further discussed below.

While almost all particles consist predominantly of one mineral, this does not mean that they occur fully liberated. The latter can be quantified by the liberation degree of a mineral, which is the ratio of the volume of this mineral that is liberated to the total volume of this mineral, as introduced in Eqs. (1) and (2). The liberation degree varies depending on particle size, as shown in Fig. 10, where smaller particles generally have a higher probability of occurring fully liberated. However, the degree of liberation only provides a simplified view on the collected data, which is also attainable by the application of standard methods, e.g., multi-stage density separation by heavy liquids or thin sectioning in the case of a mineral liberation analyser. But, since our method provides comprehensive particle-discrete data for all 22468 identified particles in the Nano-CT reconstructions, we can also plot particle and grain volume against each other, see Fig. 11, where each saxolite grain is considered individually in order to predict a possible sepa-

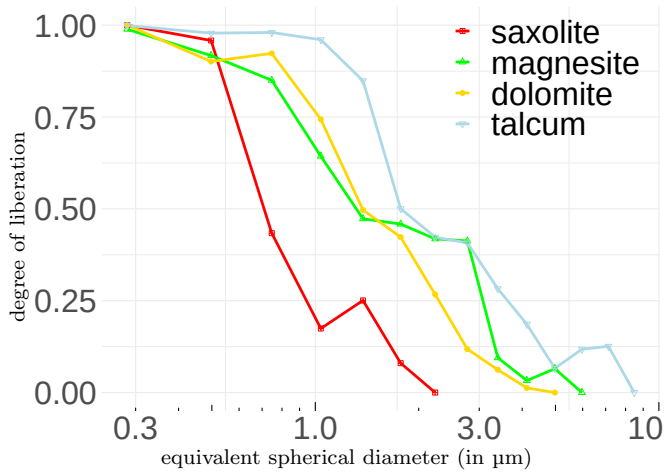

Figure 10: Volume specific liberation degree. The values at the dots are computed by means of Eq. (2) for the surrounding particle size interval.

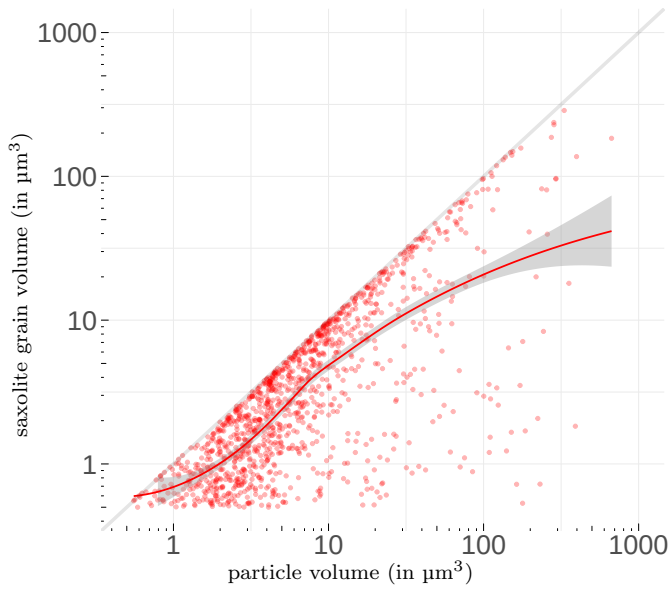

Figure 11: Grain over particle volume map targeting saxolite, which corroborates the segmentation workflow being able to analyze individual particles. The red curve illustrates the mean grain volume for a given particle volume, whereas the gray shadowing indicates the corresponding error bar.

ration process. Here, the corresponding volumes illustrate a more apprehensible relation than the sphere equivalent diameter and give hint directly to the total amount of particles that are not fully liberated. The results obtained for the other three minerals are illustrated in Fig. S7. The red curve in Fig. 11 provides an estimation of the liberation degree by its distance to the diagonal line – the farer away from the diagonal line, the lower the liberation degree. The corresponding statistical error (gray shadowing) gives hint to the reliability for each fixed particle size: the error is small in the range from 2 µm^3 to 200 µm^3 and increases for smaller and larger particles because of the resolution and FOV limits, respectively.

3.5. Scale-bridging Tomography

The analysis of the Nano-CT data results in detailed information with respect to size and mineralogical composition of the segmented particles, as depicted in Figs. 9 and 11. However, in case of a material with inhomogenously distributed particles, results derived from the analysis of Nano-CT-sized volumes might not be representative. To investigate the homogeneity of the material, the Micro-CT volume is analyzed, which delivers an approximately 60-times larger acquired sample volume compared to the three combined Nano-CT measurements. For that purpose, the particle-discrete segmentation of the Micro-CT volume, as described in Sec. 2.3.3, is decomposed into 60 pieces of the same size as a Nano-CT reconstruction. Then, distributional properties of particle sizes within each of these pieces are investigated for given size intervals, see Figure 12. In particular, for each Nano-CT-sized volume piece, the frequency of particles whose equivalent spherical diameter belongs to a certain size interval is computed. The mean values over all volume pieces and the corresponding 95 % confidence intervals are depicted in Fig. 12.

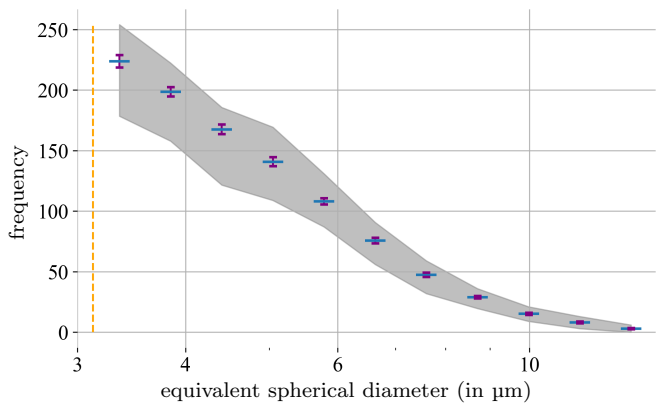

Figure 12: Distributional properties of the equivalent spherical diameter of particles in Nano-CT-sized pieces of the Micro-CT tomogram. In particular, the mean values of frequencies over all pieces are depicted as blue horizontal lines for each size interval under consideration. The corresponding standard errors are depicted by purple vertical lines and the 95 % confidence intervals are visualized in gray. The yellow vertical line represents the cut-off particle size resulting from the medium resolution of the Micro-CT scan of about 3.2 µm (each size interval comprises the diameter range surrounding each sampling point in the graph from the half-distance towards the preceding sampling point to the half-distance towards succeeding sampling point, respectively).

This visualization displays the variability of the estimated particle size distribution when considering Nano-CT-sized volumes—allowing for the assessment of the reliability of Nano-CT-based characterizations. Since the 95 % confidence intervals are small for all considered size intervals, we can conclude that all Nano-CT-sized volume pieces are similar with respect to the constituent particle sizes and number of particles without comparing the mineral composition, so that one single investigated Nano-CT volume can be considered as representative for the original Micro-CT sized sample. For further extrapolation to a bulk sample, we refer to a representative study from the Micro-CT perspective on the applied preparation workflow [19], showing the homogeneity for equally prepared samples. The lower resolution of the Micro-CT reconstruction, in contrast to the Nano-CT measurements, partly leads to wrongly-interpreted, connected particles and disregards smaller particles (below 3.2 µm). Thus, the determined total number of particles in the Nano-CT-sized volume pieces of the Micro-CT reconstruction is smaller than in corresponding Nano-CT measurements of the same volume size. Similarly, the analysis of Micro-CT reconstructions leads to a right-shifted particle size distribution.

4. Discussion

The presented workflow enables a quantitative characterization of the considered particle system with respect to particle size and composition. Note that for the compositional characterization of particles, FIB slices and SEM-EDXS analyses are required to obtain a phase segmentation of the considered volumes, see Sec. 2.3.1. Due to the divergence of the FIB beam and the subsequent curvature of the cutting plane, it is difficult to precisely associate pixels in the EDXS data with corresponding voxels in Nano-CT reconstructions. Therefore, we did not directly utilize the EDXS data itself for training the considered ML algorithm. Instead, large particles within the EDXS data have been manually identified and labeled within the Nano-CT reconstructions—which provided us with training data for the segmentation procedure.

In principle, it would be possible to slice and view (including SEM-EDXS) the whole sample volume by FIB milling (so-called slice & view FIB-SEM tomography). However, the acquisition of FIB-SEM tomography data for such large sample volumes with a high spatial resolution is a tedious and time-consuming procedure which additionally often suffers under charging effects. Our workflow demonstrates a more time-effective, alternative investigation routine using EDXS maps from only a few selected slices to inform the complete Nano-CT volume segmentation.

The limitations of the presented routine with respect to the Nano-CT experiments are the spatial resolution and the gray value range in the reconstructed volumes caused by the quasi-monochromatic beam (including noise). The lower limit of the particle size depends on the optical resolution of the Nano-CT reconstructions (about 150 nm in the used imaging mode). Due to this reason, particles with an equivalent spherical diameter smaller than two times the resolution, so <0.3 µm, were omitted in the performed analyses. The exact monochromatic filtering of the Nano-CT microscope is complex. Therefore, we provide an experimental approximation for the limitation distinguishing different mineral components according to their attenuation length difference. In this case study, the difference in the attenuation coefficients of the four minerals is large enough to be able to separate the phases well (cf. Tab. 1). For instance, the difference in the reconstructed gray values between saxolite and dolomite is 4000 corresponding to 8 µm attenuation length (see Tab. 1), which is around ten times larger than the gray value range of 400 within the saxolite phase. Similar to the particle size limit, we would suggest a minimum difference in the attenuation length resulting in a gray value difference of two times the gray value range of the individual phases, which is 800 in the case of saxolite. This value range approximately equals an attenuation length difference of ±1.6 µm, meaning that all phases with a higher difference in gray value or attenuation length should be distinguishable in the case of this Nano-CT instrument and the applied imaging conditions.

Note that the applied Nano-CT instrument is not able to image the whole 400 µm sample due to its limited field of view and the absorption length of the employed X-ray energy. Therefore, if the sample was inhomogeneous, the analysis of Nano-CT data could lead to unrepresentative results. In order to verify homogeneity of the sample, the available Micro-CT image data was analyzed regarding the representability of Nano-CT sized volumes. More precisely, Nano-CT-sized volumes taken from the Micro-CT volume indicate similar particle size distributions, see Fig. 12. Therefore, we assume that the position of the Nano-CT measurements in the considered sample has a marginal impact on the results. This is further corroborated by observing a similar trend of the particle size distributions above 3 µm equivalent spherical diameter for the investigated Micro-CT and Nano-CT reconstructions (cf. Figs. 9 and 12). However, we expect an overall shift towards larger particle sizes due to the reduced resolution in the Micro-CT volume.

As described in Sec. 2.1, the mixture was intentionally prepared with the volume ratio of 30 to 70 (talcum to saxolite). Our workflow enables us to determine the volume ratio from reconstructed 3D image data. More precisely, since we can assign for each voxel in the Nano-CT data the corresponding mineralogical phase, we can compute the phase volume fractions, which leads to a volume ratio of 73 to 27 (talcum to saxolite). This is in good agreement with an inadvertently prepared ratio of 70 to 30, and not as expected 30 to 70. Although a precise quantification of the acquired EDXS maps from single slices (cf. Figs. 6(b) and 7(a and d)) w.r.t. the volumetric presence of the distinct minerals is difficult to pursue, e.g., due to

the inclined sample geometry and the detector position (absorption correction), the EDXS maps rather indicate a ratio of 70:30. This is further supported by the determined area ratio of the segmented saxolite regions in the EDXS maps w.r.t. the talcum phases (average area ratio of 65:35 for three EDXS maps in Fig. 7(d)). Assuming a sample was prepared as 70 to 30 and considering that, according to the manufacturer, the original saxolite powder also contains talcum (4 %), the actual volume ratio of the mixture should be 71.2 and 28.8 which matches the estimated result obtained from image data even better, demonstrating the precision of the presented workflow.

The particle-wise segmentation of the Nano-CT reconstructions is based on a convolutional neural network, and thus, the network's output is unpredictable for images that exhibit novel features not seen before in the training data. For the current data set, it was possible to encompass relevant features by labeling just three slices, but this might not be possible for image data with more diverse images and features. In addition, while errors caused by over-segmentation are negligible within our particle-wise segmentation (observed through visual inspection), under-segmentation can occur especially when small particles are involved. Since we consider volume-weighted descriptors, this type of under-segmentation should not significantly influence the results. However, the occurrence of composite particles is overestimated as under-segmentation might occur for neighboring particles composed of different minerals. To account for this, particles which have a volume fraction greater than 0.99 for any mineral were considered to be fully liberated.

In comparison to common chemical analyses, the additional particle-discrete information extracted from our correlative workflow offers enhanced knowledge on the investigated materials. For example, note that in mineral processing similar particle systems occur as a result of particle milling processes which are subsequent to the mineral excavation to increase the LD of the material. Thus, on the basis of the derived particle-size related data, it is possible to adjust the applied particle milling process if the required LD of the minerals is reached at a certain particle size. For that purpose, the degree of liberation was analyzed for different minerals and particle sizes. In particular, for saxolite the degree of liberation decreases for particles larger than 0.5 µm, as shown in Fig. 10. Such a trend is expected due to the higher stability of single grained particles and it can guide towards an optimized choice of the milling size. More specifically, if a high degree of liberation is desired for saxolite, further milling might be necessary to increase the LD.

5. Conclusions

In summary, the presented correlative characterization workflow over multiple length scales is utilized to unambiguously allocate and identify different constituent mineral types contained as grains in similarly sized particles. This can be a challenging task for common mineralogical characterization methods which rely on only particle sizes. In particular, a large volume was reconstructed and analyzed in 3D with various imaging techniques, in order to ascertain a comprehensive characterization of the particles' size and composition. Our presented correlative 3D characterization approach is suitable to be applied to particulate samples with primary particle sizes in the range of 0.3 µm to 15 µm by considering resolution and FOV limits of the Nano-CT instrument. In our study, the morphology and composition are available for each individual particle and can be evaluated to directly compute the particle-wise mineral liberation, which usually cannot be determined using standard methods for particle characterization. The combination of multiple imaging techniques significantly improves the statistical relevance (high number of particles) and segmentation precision (high resolution) compared to the application of a single technique. The proposed method provides multidimensional particle properties enabling a more detailed understanding of multidimensional separation processes, see [39]. In a forthcoming study, the presented characterization workflow is supposed to be deployed to evaluate the separation efficiency achieved by a combination of deflector wheel classifier and triboelectric charge sorting. Furthermore, the determined mineral liberation degree properties will allow tuning processes to obtain optimized milling degrees of the original mineral batches. Moreover, the data obtained with the presented approach can be used as input for numerical simulations to obtain a detailed understanding of these complex separation processes.

Data Availability

The reconstructed image data, in this case, TIFF stacks, the related acquisition and reconstruction parameters are stored within the scientific data repository of Technische Universität Dresden and TU Bergakademie Freiberg with all relevant meta-data [40].

Acknowledgments

We thank Janis Wirth for support with the graphical abstract and Tatiana Kormilina, Johannes Voss and Simon Carl for support with the phase segmentation of the data sets. The authors thank the German Research Foundation (DFG) for supporting this study as part of the priority program SPP 2045 (DFG project number: 313858373), which is dealing with highly specific multidimensional separation of technical ultra–fine particle systems with particle sizes below 10 µm, for funding of the micro-CT (INST 267/129-1), the financial support within the frameworks of the research training group GRK1896 "In situ Microscopy with Electrons, X-rays and Scanning Probes" (Project-ID: 218975129), the project SP648/8 "High-resolution X-ray microscopy for correlative tomography, high throughput

screening and in situ mechanical testing of structural and functional materials" (Project-ID 316992193), the Collaborative Research Centres 1411 "Design of Particulate Products" (Project-ID 416229255) and 1452 "Catalysis at Liquid Interfaces" (Project-ID 431791331).

References

1. Radetzki, M.. Metal mineral resource exhaustion and the threat to material progress: The case of copper. *World Development* 1975;3(2-3):123–136. doi:10.1016/0305-750x(75)90042-x.
2. Arndt, N.T., Fontboté, L., Hedenquist, J.W., Kesler, S.E., Thompson, J.F.H., Wood, D.G.. Future global mineral resources. *Geochemical Perspectives* 2017;:1–171doi:10.7185/geochempersp.6.1.
3. Cook, N., Ciobanu, C., Ehrig, K., Slattery, A., Verdugo-Ihl, M., Courtney-Davies, L., Gao, W.. Advances and opportunities in ore mineralogy. *Minerals* 2017;7(12):233. doi:10.3390/min7120233.
4. Stramski, D., Sedlák, M.. Application of dynamic light scattering to the study of small marine particles. *Applied Optics* 1994;33(21):4825–4834. URL: http://opg.optica.org/ao/abstract.cfm?URI=ao-33-21-4825. doi:10.1364/AO.33.004825.
5. Brown, D.J., Vickers, G.T., Collier, A.P., Reynolds, G.K.. Measurement of the size, shape and orientation of convex bodies. *Chemical Engineering Science* 2005;60(1):289–292. doi:10.1016/j.ces.2004.07.056.
6. Gaudin, A.M.. Principles of Mineral Dressing. McGraw–Hill Book Company, Inc.; 1939.
7. Macho, O., Kabát, J., Gabrišová, L., Peciar, P., Juriga, M., Fekete, R., Galbavá, P., Blaško, J., Peciar, M.. Dimensionless criteria as a tool for creation of a model for predicting the size of granules in high–shear granulation. *Particulate Science and Technology* 2019;38(3):381–390. doi:10.1080/02726351.2018.1548531.
8. Stock, S.R.. Recent advances in X–ray microtomography applied to materials. *International Materials Reviews* 2008;53(3):129–181. doi:10.1179/174328008x277803.
9. Ketcham, R.A., Carlson, W.D.. Acquisition, optimization and interpretation of X–ray computed tomographic imagery: Applications to the geosciences. *Computers and Geosciences* 2001;27(4):381–400. doi:10.1016/S0098-3004(00)00116-3.
10. Wang, Y., Miller, J.D.. Current developments and applications of micro-CT for the 3D analysis of multiphase mineral systems in geometallurgy. *Earth-Science Reviews* 2020;211:103406. doi:10.1016/j.earscirev.2020.103406.
11. Miller, J.D., Lin, C.L., Cortes, A.B.. A review of X–ray computed tomography and its applications in mineral processing. *Mineral Processing and Extractive Metallurgy Review* 1990;7(1):1–18. doi:10.1080/08827509008952663.
12. Lin, C.L., Miller, J.D., Cortes, A.. Applications of X–ray computed tomography in particulate systems. *KONA Powder and Particle Journal* 1992;10(0):88–95. doi:10.14356/kona.1992013.
13. Pavlinsky, G.V.. Fundamentals of X-ray Physics. Cambridge International Science Publishing; 2008. ISBN 1904602649.
14. Buzug, T.M.. Computed Tomography from Photon Statistics to Modern Cone–beam CT. Springer; 2008. doi:10.1007/978-3-540-39408-2.
15. Withers, P.J., Bouman, C., Carmignato, S., Cnudde, V., Grimaldi, D., Hagen, C.K., Maire, E., Manley, M., du Plessis, A., Stock, S.R.. X–ray computed tomography. *Nature Reviews Methods Primers* 2021;1(1). doi:10.1038/s43586-021-00015-4.
16. Reyes, F., Lin, Q., Cilliers, J.J., Neethling, S.J.. Quantifying mineral liberation by particle grade and surface exposure using X–ray microCT. *Minerals Engineering* 2018;125:75–82. doi:10.1016/j.mineng.2018.05.028.
17. Schulz, B., Sandmann, D., Gilbricht, S.. SEM-based automated mineralogy and its application in geo- and material sciences. *Minerals* 2020;10(11):1004. doi:10.3390/min10111004.
18. Heinig, T., Bachmann, K., Tolosana-Delgado, R., van den Boogaart, G., Gutzmer, J.. Monitoring gravitational and particle shape settling effects on MLA sample preparation. In: *IAMG Conference, Freiberg, Germany*. 2015:.
19. Ditscherlein, R., Leißner, T., Peuker, U.A.. Preparation strategy for statistically significant micrometer–sized particle systems suitable for correlative 3D imaging workflows on the example of X–ray microtomography. *Powder Technology* 2022;395:235–242. doi:10.1016/j.powtec.2021.09.038.
20. Ueda, T.. Experimental study on the stereological bias in surface exposure measurement of ore particles. *Advanced Powder Technology* 2020;31(1):61–69. doi:10.1016/j.apt.2019.09.037.
21. Ueda, T., Oki, T., Koyanaka, S.. Experimental analysis of mineral liberation and stereological bias based on X–ray computed tomography and artificial binary particles. *Advanced Powder Technology* 2018;29(3):462–470. doi:10.1016/j.apt.2017.11.004.
22. Xing, B., Fan, W., Lyu, Y., Sun, H., Che, J.. Influence of particle mineralogy and size on the morphological characteristics of mineral fillers. *Journal of Materials Research and Technology* 2021;15:3995–4009. URL: https://www.sciencedirect.com/science/article/pii/S2238785421011625. doi:https://doi.org/10.1016/j.jmrt.2021.10.026.
23. Kyle, J.R., Ketcham, R.A.. Application of high resolution X–ray computed tomography to mineral deposit origin, evaluation, and processing. *Ore Geology Reviews* 2015;65:821–839. doi:10.1016/j.oregeorev.2014.09.034.
24. Sittner, J., Da Assuncao Godinho, J.R., Renno, A., Cnudde, V., Boone, M., de Schryver, T., van Loo, D., Merkulova, M., Roine, A., Liipo, J.. Spectral x-ray computed micro tomography: 3-dimensional chemical imaging. *X-Ray Spectrometry* 2020;50(2):92–105. doi:10.1002/xrs.3200.
25. Godinho, J.R.A., Westaway-Heaven, G., Boone, M.A., Renno, A.D.. Spectral tomography for 3D element detection and mineral analysis. *Minerals* 2021;11(6):598. doi:10.3390/min11060598.
26. Furat, O., Leißner, T., Ditscherlein, R., Šedivý, O., Weber, M., Bachmann, K., Gutzmer, J., Peuker, U.A., Schmidt, V.. Description of ore particles from X–ray microtomography (XMT) images, supported by scanning electron microscope (SEM)–based image analysis. *Microscopy and Microanalysis* 2018;24(5):461–470. doi:10.1017/s1431927618015076.
27. Hansen, L., Wollmann, A., Weers, M., Benker, B., Weber, A.P.. Triboelectric charging and separation of fine powder mixtures. *Chemical Engineering & Technology* 2020;43(5):933–941. doi:10.1002/ceat.201900558.
28. Kyrieleis, A., Titarenko, V., Ibison, M., Connolley, T., Withers, P.J.. Region–of–interest tomography using filtered backprojection: Assessing the practical limits. *Journal of Microscopy* 2010;241(1):69–82. doi:10.1111/j.1365-2818.2010.03408.x.
29. van Aarle, W., Palenstijn, W.J., De Beenhouwer, J., Altantzis, T., Bals, S., Batenburg, K.J., Sijbers, J.. The astra toolbox: A platform for advanced algorithm development in electron tomography. *Ultramicroscopy* 2015;157:35–47. URL: https://www.sciencedirect.com/science/article/pii/S0304399115001060. doi:https://doi.org/10.1016/j.ultramic.2015.05.002.
30. van Aarle, W., Palenstijn, W.J., Cant, J., Janssens, E., Bleichrodt, F., Dabravolski, A., Beenhouwer, J.D., Batenburg, K.J., Sijbers, J.. Fast and flexible X-ray tomography using the ASTRA toolbox. *Optics Express* 2016;24(22):25129–25147. URL: http://opg.optica.org/oe/abstract.cfm?URI=oe-24-22-25129. doi:10.1364/OE.24.025129.
31. Palenstijn, W., Batenburg, K., Sijbers, J.. Performance improvements for iterative electron tomography reconstruction using graphics processing units (GPUs). *Journal of Structural Biology* 2011;176(2):250–253. URL: https://www.sciencedirect.

com/science/article/pii/S1047847711002267. doi:https://doi.org/10.1016/j.jsb.2011.07.017.

32. Ditscherlein, R., Furat, O., de Langlard, M., Martins de Souza e Silva, J., Sygusch, J., Rudolph, M., Leißner, T., Schmidt, V., Peuker, U.A.. Multiscale tomographic analysis for micron–sized particulate samples. *Microscopy and Microanalysis* 2020;26(4):676–688. doi:10.1017/s1431927620001737.
33. Lenz, M., Wirth, J., Englisch, S., Rosiwal, J., Buchinger, N., Weiser, M., Virtanen, S., Apeleo Zubiri, B., Spiecker, E.. Correlative nano-computed tomography and focused ion-beam sectioning: A case study on a co-base superalloy oxide scale. *Advanced Engineering Materials* 2020;22(9):1900823. URL: https://onlinelibrary.wiley.com/doi/abs/10.1002/adem.201900823. doi:https://doi.org/10.1002/adem.201900823. arXiv:https://onlinelibrary.wiley.com/doi/pdf/10.1002/adem.201900823.
34. Sommer, C., Straehle, C., Koethe, U., Hamprecht, F.A.. Ilastik: Interactive learning and segmentation toolkit. In: *2011 IEEE international Symposium on Biomedical Imaging: From nano to macro*. IEEE; 2011:230–233.
35. Rezatofighi, H., Tsoi, N., Gwak, J., Sadeghian, A., Reid, I., Savarese, S.. Generalized intersection over union: A metric and a loss for bounding box regression. In: *Proceedings of the IEEE/CVF conference on computer vision and pattern recognition*. 2019:658–666.
36. Çiçek, Ö., Abdulkadir, A., Lienkamp, S.S., Brox, T., Ronneberger, O.. 3D U-net: Learning dense volumetric segmentation from sparse annotation. In: Ourselin, S., Joskowicz, L., Sabuncu, M.R., Unal, G., Wells, W., eds. *Medical Image Computing and Computer-Assisted Intervention – MICCAI 2016*. Springer International Publishing. ISBN 978-3-319-46723-8; 2016:424–432.
37. Furat, O., Kirstein, T., Leißner, T., Bachmann, K., Gutzmer, J., Peuker, U.A., Schmidt, V.. Multidimensional characterization of particle morphology and mineralogical composition using ct data and r-vine copulas. 2023. URL: https://arxiv.org/abs/2301.07587. doi:10.48550/ARXIV.2301.07587.
38. Soille, P.. Morphological Image Analysis: Principles and Applications. Springer; 2003. ISBN 978-3-540-42988-3.
39. Schach, E., Buchmann, M., Tolosana-Delgado, R., Leißner, T., Kern, M., van den Boogaart, G., Rudolph, M., Peuker, U.A.. Multidimensional characterization of separation processes. Part 1: Introducing kernel methods and entropy in the context of mineral processing using SEM-based image analysis. *Minerals Engineering* 2019;137:78–86. URL: https://www.sciencedirect.com/science/article/pii/S0892687519301499. doi:https://doi.org/10.1016/j.mineng.2019.03.026.
40. Ditscherlein, R.. 3 tomographic data sets of nano-CT measurements of a 30:70 vol-% mixture of talcum and saxolite. 2022. doi:http://dx.doi.org/10.25532/OPARA-186.